Available online at www.sciencedirect.com
SCIENCE DIRECT®
Journal of Sound and Vibration 292 (2006) 881–898
JOURNAL OF SOUND AND VIBRATION
www.elsevier.com/locate/jsvi

One-dimensional dynamic microslip friction model

Ender Cigeroglu, Wangming Lu, Chia-Hsiang Menq*

Department of Mechanical Engineering, The Ohio State University, Columbus OH 43202, USA

Received 17 December 2004; received in revised form 5 August 2005; accepted 13 September 2005
Available online 8 November 2005

Abstract

A one-dimensional dynamic microslip friction model, including the damper inertia, is presented in this paper. An analytical approach is developed to obtain the steady-state solution of the resulting nonlinear partial differential equations when subjected to harmonic excitation. In the proposed approach, according to the excitation frequency, a single mode of the system is considered in the steady-state solution for simplicity; consequently, phase difference among spatially distributed points is neglected. Three types of normal load distributions, resulting in distinct stick–slip transitions along the contact interface, are studied. The resulting hysteresis curves and the associated Fourier coefficients are obtained and compared with each other. An equivalent point contact friction model is established and compared with the proposed microslip model, illustrating the effects of partial slip in the contact interface for low amplitude or high normal load applications.

1. Introduction

In the dynamic response analysis of structures having friction contact, two types of approaches are used, the macroslip and the microslip methods. Due to its mathematical simplicity, the macroslip approach [1–5] is widely used, in which the friction interface is modeled as a rigid body, and is entirely in slip or stick states. This method is acceptable if gross-slip occurs at the friction interface, which is possible if the normal load acting on the interface is small. On the other hand, the microslip method [6–10] is mathematically complicated; however, since the friction interface is modeled as an elastic body, it is capable of modeling partial slip, which occurs if the normal load acting on the interface is high. For those cases, macroslip model results in stuck interface and estimates no energy dissipation through friction contact.

Menq et al. [6] developed a microslip model, in which the friction damper was modeled as an elastic bar in contact with a rigid ground and connected to a spring at the left end. A shear layer was included between the bar and the ground; therefore, it is possible to have linear deformation relative to the support before the beginning of slip [11]. Under the effect of uniform normal load distribution, partial-slip and gross-slip of the bar were studied. A single-degree-of-freedom oscillator with a friction damper was analyzed by applying the Harmonic Balance Method (HBM), and the authors assessed that for high normal load cases this microslip

*Corresponding author. Tel./fax: +1 614 292 4232.
E-mail address: menq.1@osu.edu (C.-H. Menq).

0022-460X/$ - see front matter © 2005 Elsevier Ltd. All rights reserved.
doi:10.1016/j.jsv.2005.09.019

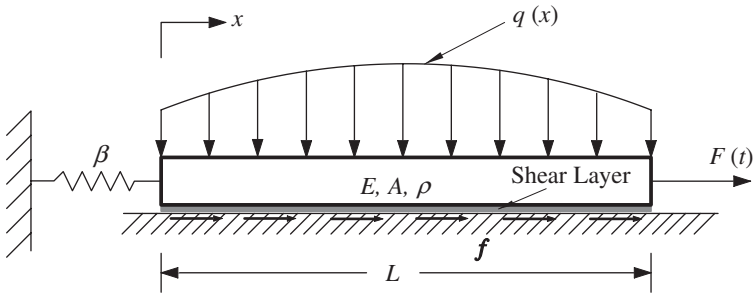

Fig. 1. One-dimensional microslip model.

model showed approximately 50 percent reductions in the resonant response. In addition to this, Menq et al. [8] explained experimental friction damping data by using this microslip friction model.

Csaba [9] proposed a microslip friction model with a quadratic normal load distribution based on the model developed by Menq et al. [6] in which the shear layer was removed for simplicity. A single blade with a friction damper attached to the ground was analyzed in the frequency domain and the author evaluated that macroslip predicted the response amplitudes much higher than the microslip model used. Filippi et al. [12] described a measurement method in order to determine the friction characteristics between two surfaces. The authors estimated the possible measurement errors and tried to eliminate or avoid them in the measurement process. Specimens were selected in order to have negligible inertial effects and hysteresis curves for different displacement amplitudes were given which showed the microslip behavior. Friction coefficient between the surfaces and contact stiffness in the direction of motion was also determined through the experiment. Song et al. [13] added a parallel spring to the parallel-series Iwan model and used this model to estimate the friction in the joints. The model parameters estimating the microslip behavior were determined from experimental results by applying a neural network algorithm.

The objective of this study is to develop a dynamic one-dimensional microslip friction model by including the inertia of the damper. For this purpose a one-dimensional beam model which is similar to the one introduced by Menq et al. [6], but includes the inertia of the beam and has a non-uniform normal load distribution, is proposed and is shown in Fig. 1. The beam is connected to the ground from the left end with a spring in order to include strain hardening effects, and a harmonic excitation is applied to the right end of the beam. A shear layer, which permits elastic deformation of the beam before the occurrence of slip, is inserted between the beam and the ground. The shear layer can be visualized as distributed springs connected to the beam and in contact with the ground, and obeying the Coulomb friction law with a constant friction coefficient throughout the length of the beam. Since this is a one-dimensional model normal load applied on the beam is assumed to be directly transmitted to the shear layer. The system is analyzed for uniform, and convex and concave normal load distributions, which result in distinct stick–slip transitions along the contact interface.

In the remaining parts of this paper, determination of stick–slip transitions along the contact interface for different normal load distributions is presented and force displacement relationships for constant, convex and concave normal load distributions are derived. The effect of excitation frequency is analyzed and results obtained for different normal load distributions are compared with each other and with a representative point contact model.

2. Determination of stick–slip transitions

An analytical approach is developed to determine the stick–slip transitions of the steady-state solution of the frictionally constrained system when subjected to harmonic excitation. In the proposed approach, according to the excitation frequency single mode of the system is considered in the steady-state solution for simplicity; consequently, the phase difference among spatially distributed points is neglected.

2.1. Determination of contact elastic force

In order to determine stick–slip transition in the microslip model proposed in Fig. 1, the build-up of elastic force along the contact interface between the beam and the ground is first examined. As a starting point, the microslip model is analyzed assuming the beam is completely stuck and the contact elastic force obtained through this analysis is used to determine the effects of damper inertia. In conjunction with the normal load distribution, it will later be employed to determine the transitions between stick and slip, and to obtain the resulting friction force. The equations of motion for the completely stuck beam can be written as

$$EA\,\frac{\partial^2 u}{\partial x^2} - ku = \rho A\omega^2\,\frac{\partial^2 u}{\partial \theta^2}, \tag{1}$$

with the following boundary conditions

$$EA\,\frac{\partial u}{\partial x}\bigg|_{x=0} = \beta u(0,\theta), \quad EA\,\frac{\partial u}{\partial x}\bigg|_{x=L} = F_0\sin(\theta), \tag{2}$$

where ω, t, E, ρ, A, L and k are excitation frequency, time, modulus of elasticity, density, cross-sectional area, length and the shear layer stiffness of the beam, respectively, and $\theta = \omega t$. Solving the partial differential equation analytically, the contact elastic force acting on the beam can be obtained. The spatial distribution of the resulting contact elastic force for different excitation frequencies is given in Fig. 2 to illustrate the effects of damper inertia, and is seen to be similar to the mode shape of the constrained beam. Moreover, Fig. 3 shows the build-up of the contact elastic force, together with three different normal load distributions, while increasing the amplitude of low-frequency excitation. It is seen that as the excitation amplitude increases the contact elastic force generated in the shear layer becomes larger than the allowable value, depending on the normal load, and the contact interface starts to slip at a location depending on the distribution of normal load. For the example shown in Fig. 3, the contact interface starts to slip at the right end of the beam for both the constant and the convex normal load distributions; whereas it starts to slip somewhere around the middle of the beam for the concave normal load distribution. It can also be concluded that for the first vibration mode both the constant and the convex normal load distributions lead to similar stick–slip transition along the friction interface, which is a stick region at the left side and a slip region at the right side. The slip region propagates towards the left end of the beam, reverses and repeats. Since showing similar stick–slip transition, they are analyzed together, where the case of constant normal load is considered as a special case of the convex

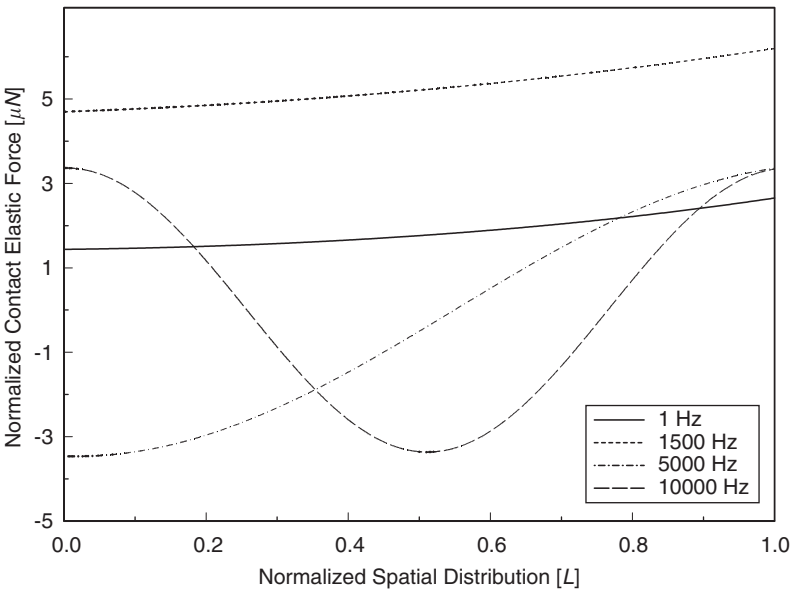

Fig. 2. Effect of excitation frequency on contact elastic force: ———, 1 Hz; - - - - - -, 1500 Hz; - - - - - - - - - - - -, 5000 Hz; — — — — —, 10 000 Hz.

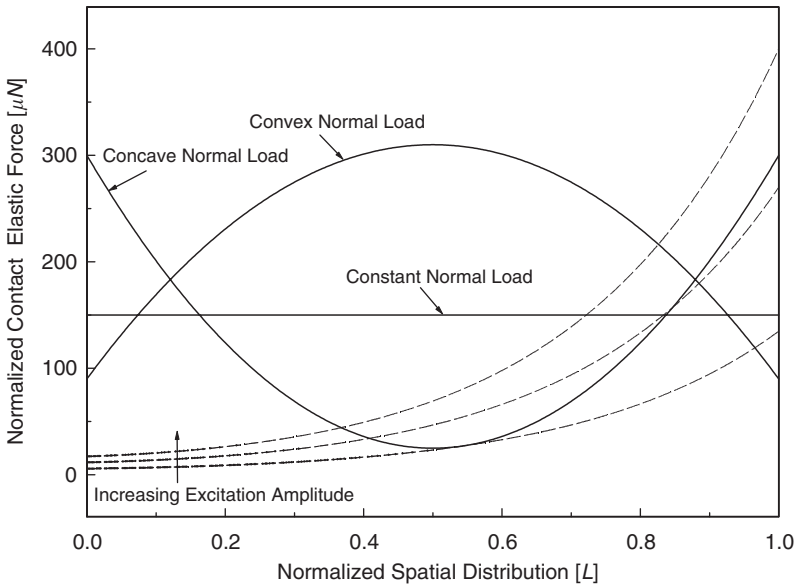

Fig. 3. Build up of contact elastic force and its comparison with various normal load distributions: ———, normal load distribution; ------, contact elastic force.

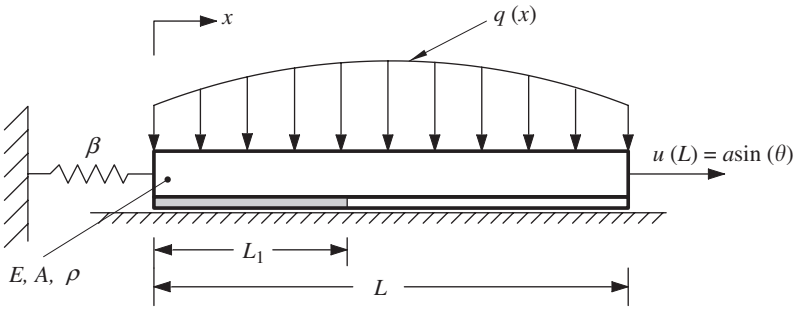

Fig. 4. Two-region friction interface due to convex normal load distribution.

normal load distribution. On the other hand, for the case of concave normal load distribution, the stick–slip transition along the friction interface is composed of two stick regions at the left and the right sides of the beam, and in-between is a slip region, which propagates towards the right and the left ends of the beam, reverses and repeats.

2.2. Two-region friction interface

It is concluded in Section 2.1 that, as the amplitude of the excitation force at the right end of the beam increases, convex normal load distribution results in a two-region friction interface, a stuck region on the left side and a slip region on the right. Fig. 4 shows the microslip model with a two-region friction interface where, L_1 is the length of the stuck region and $q(x)$ is the normal load distribution over the interface. Since it is aimed to obtain hysteresis curves, instead of force input, displacement input is used in the model. The nonlinear partial differential equations defining this system are given as

$$EA\frac{\partial^2 u}{\partial x^2} - k(u(x,\theta) - w(x)) = \rho A\omega^2 \frac{\partial^2 u}{\partial \theta^2}, \quad 0 \leqslant x \leqslant L_1, \tag{3}$$

$$EA\frac{\partial^2 u}{\partial x^2} - \operatorname{sgn}\left(\frac{\partial u}{\partial \theta}\right)\mu q(x) = \rho A\omega^2\frac{\partial^2 u}{\partial \theta^2}, \quad L_1 \leqslant x \leqslant L, \tag{4}$$

with the boundary and compatibility conditions

$$EA\left.\frac{\partial u}{\partial x}\right|_{x=0} = \beta u(0,\theta), \quad u(L,\theta) = a\sin(\theta), \tag{5}$$

$$u(L_1^-,\theta) = u(L_1^+,\theta), \quad \left.\frac{\partial u}{\partial x}\right|_{L_1^-} = \left.\frac{\partial u}{\partial x}\right|_{L_1^+}, \tag{6}$$

where μ is the friction coefficient and $w(x)$ is the displacement of the shear layer at the time of sticking, and for the regions which have not slipped, $w(x) = 0$. In Eqs. (3), (4) and (6), L_1 is still an unknown; however, it should be noted that the friction force calculated at $x = L_1$ from Eqs. (3) and (4) should be the same, therefore equating these friction forces results in the equation

$$|k(u(L_1,\theta) - w(L_1))| = \mu q(L_1), \tag{7}$$

from which L_1, the change of stick–slip regions, can be determined. Eqs. (3) and (4) for θ between 0 and $\pi/2$ can be rewritten as

$$EA\frac{\partial^2 u}{\partial x^2} - ku = \rho A\omega^2\frac{\partial^2 u}{\partial \theta^2} \quad 0 \leqslant x \leqslant L_1, \tag{8}$$

$$EA\frac{\partial^2 u}{\partial x^2} - \mu q(x) = \rho A\omega^2\frac{\partial^2 u}{\partial \theta^2} \quad L_1 \leqslant x \leqslant L, \tag{9}$$

where $w(x)$ is taken as zero for the points that have not been slipped as pointed out formerly. It should be noted that, Eqs. (8) and (9) are linear and the solution can be obtained in terms of L_1 if u is taken in the following form

$$u = \begin{cases} u_1(x) + u_2(x,\theta), & 0 \leqslant \theta \leqslant L_1, \\ v_1(x) + v_2(x,\theta), & L_1 \leqslant \theta \leqslant L. \end{cases} \tag{10}$$

Since only the first mode of the beam is considered, there is no phase difference between the points throughout the length; hence, inserting Eq. (10) into Eqs. (8) and (9) yields the results

$$\begin{aligned} u_1(x) &= D_1\sinh(\lambda x) + D_2\cosh(\lambda x), \\ u_2(x,\theta) &= (C_1\sinh(\gamma x) + C_2\cosh(\gamma x))\sin(\theta), \\ v_1(x) &= Q(x) + c_1 x + c_0, \\ v_2(x,\theta) &= (C_3\sin(\alpha x) + C_4\cos(\alpha x))\sin(\theta), \end{aligned} \tag{11}$$

where

$$\lambda = \sqrt{\frac{k}{EA}}, \quad \alpha = \omega\sqrt{\frac{\rho}{E}}, \quad \gamma = \sqrt{\frac{k}{EA} - \frac{\rho}{E}\omega^2}. \tag{12}$$

The unknown coefficients in Eq. (11) are in terms of L_1 and can be determined using the boundary and the compatibility conditions (5) and (6), respectively. Using Eq. (7) together with Eqs. (11) and (12), a nonlinear equation for L_1 is obtained and given as

$$\left[\frac{\mu q(L_1)}{kEA\alpha} + \frac{Q'(L_1)(L-L_1) + Q(L) - Q(L_1)}{EA\alpha + \beta'\alpha(L-L_1)}\right]EA\cos[\alpha(L-L_1)] + \beta'\sin[\alpha(L-L_1)] - a\sin(\theta) = 0, \tag{13}$$

where

$$\beta' = \beta'(L_1) = EA\gamma\,\frac{EA\gamma\sinh(\gamma L_1) + \beta\cosh(\gamma L_1)}{EA\gamma\cosh(\gamma L_1) + \beta\sinh(\gamma L_1)}, \tag{14}$$

$$Q(x) = \int_0^x Q'(\xi)\,\mathrm{d}\xi, \quad Q'(x) = \int_0^x \frac{\mu}{EA}\, q(\xi)\,\mathrm{d}\xi. \tag{15}$$

It should be noted that Eq. (13) is nonlinear and an analytical solution for L_1 cannot be obtained; however, it is possible to solve θ analytically for L_1 varying between 0 and L. The solution of Eqs. (3) and (4) for θ between 0 and $\pi/2$ gives the loading curve of the resulting hysteresis loop, and Menq et al. [6] showed that if the loading curve of an elastic element is known and if the normal load distribution is time invariant it is possible to construct the hysteresis curve for cyclic motion from this result. Applying this approach, the hysteresis curve for a cycle is constructed, and the effect of excitation amplitude and frequency are analyzed and the results are presented in Section 3.

2.3. Three-region friction interface

It is concluded in Section 2.1 that a concave normal load distribution results in a three-region friction interface composed of two stick regions at the left and right sides and a slip region at the middle of the beam. The microslip model for this case is given in Fig. 5, where L_1, L_2 and $q(x)$ are the length of the stuck region on the left side, the beginning of the stuck region on the right side, and the normal load distribution over the interface, respectively. The nonlinear partial differential equations defining this system are given as

$$EA\,\frac{\partial^2 u}{\partial x^2} - k(u(x,\theta) - w(x)) = \rho A\omega^2\,\frac{\partial^2 u}{\partial \theta^2}, \quad 0 \leqslant x \leqslant L_1, \tag{16}$$

$$EA\,\frac{\partial^2 u}{\partial x^2} - \operatorname{sgn}\left(\frac{\partial u}{\partial \theta}\right)\mu q(x) = \rho A\omega^2\,\frac{\partial^2 u}{\partial \theta^2}, \quad L_1 \leqslant x \leqslant L_2, \tag{17}$$

$$EA\,\frac{\partial^2 u}{\partial x^2} - k(u(x,\theta) - w(x)) = \rho A\omega^2\,\frac{\partial^2 u}{\partial \theta^2}, \quad L_2 \leqslant x \leqslant L, \tag{18}$$

with the boundary and compatibility conditions

$$EA\,\left.\frac{\partial u}{\partial x}\right|_{x=0} = \beta u(0,\theta), \quad u(L,\theta) = a\sin(\theta), \tag{19}$$

$$\begin{aligned} u(L_1^-,\theta) &= u(L_1^+,\theta), \quad \left.\frac{\partial u}{\partial x}\right|_{L_1^-} = \left.\frac{\partial u}{\partial x}\right|_{L_1^+}, \\ u(L_2^-,\theta) &= u(L_2^+,\theta), \quad \left.\frac{\partial u}{\partial x}\right|_{L_2^-} = \left.\frac{\partial u}{\partial x}\right|_{L_2^+}, \end{aligned} \tag{20}$$

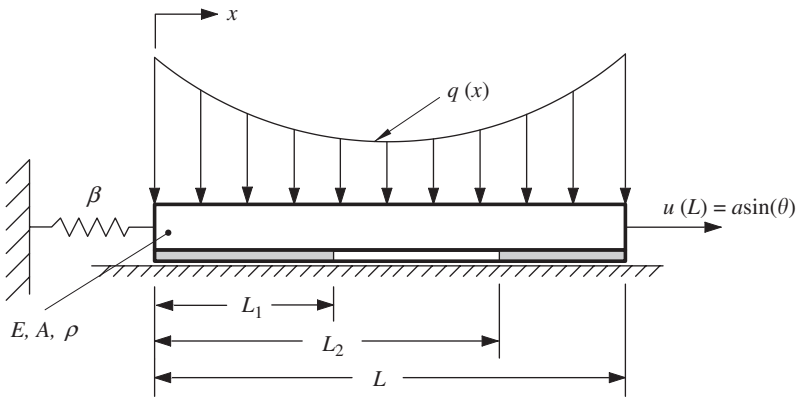

Fig. 5. Three-region friction interface due to concave normal load distribution.

where $w(x)$ is the same as in Section 2.2. It should be noted that in Eqs. (16), (17), (18) and (20) L_1 and L_2 are unknowns and in order to determine them, the friction force calculated at $x = L_1$ from Eqs. (16) and (17), and the friction force calculated at $x = L_2$ from Eqs. (17) and (18) are equated, respectively, resulting in the equations

$$|k(u(L_1,\theta) - w(L_1))| = \mu q(L_1),$$
$$|k(u(L_2,\theta) - w(L_2))| = \mu q(L_2). \tag{21}$$

Following a similar procedure as described in Section 2.2, Eqs. (16), (17) and (18) become

$$EA\frac{\partial^2 u}{\partial x^2} - ku = \rho A\omega^2 \frac{\partial^2 u}{\partial \theta^2}, \quad 0 \leqslant x \leqslant L_1, \tag{22}$$

$$EA\frac{\partial^2 u}{\partial x^2} - \mu q(x) = \rho A\omega^2 \frac{\partial^2 u}{\partial \theta^2}, \quad L_1 \leqslant x \leqslant L_2 \tag{23}$$

$$EA\frac{\partial^2 u}{\partial x^2} - ku = \rho A\omega^2 \frac{\partial^2 u}{\partial \theta^2}, \quad L_2 \leqslant x \leqslant L. \tag{24}$$

These equations are linear and the solutions are in terms of L_1 and L_2. If u is taken in the form

$$u = \begin{cases} u_1(x) + u_2(x,\theta), & 0 \leqslant x \leqslant L_1, \\ v_1(x) + v_2(x,\theta), & L_1 \leqslant x \leqslant L_2, \\ w_1(x) + w_2(x,\theta), & L_2 \leqslant x \leqslant L, \end{cases} \tag{25}$$

and only the first mode is considered, inserting Eq. (25) into Eqs. (22)–(24) leads to the solution

$$\begin{aligned} u_1(x) &= D_1 \sinh(\lambda x) + D_2 \cosh(\lambda x), \\ u_2(x,\theta) &= (C_1 \sinh(\gamma x) + C_2 \cosh(\gamma x)) \sin(\theta), \\ v_1(x) &= Q(x) + c_1 x + c_0, \\ v_2(x,\theta) &= (C_3 \sin(\alpha x) + C_4 \cos(\alpha x)) \sin(\theta), \\ w_1(x) &= D_3 \sinh(\lambda x) + D_4 \cosh(\lambda x), \\ w_2(x,\theta) &= (C_5 \sinh(\gamma x) + C_6 \cosh(\gamma x)) \sin(\theta), \end{aligned} \tag{26}$$

where α, γ and λ are given in Eq. (12). The unknown coefficients in Eq. (26) are in terms of L_1 and L_2, and can be determined by applying the boundary and the compatibility conditions given in Eqs. (19) and (20), respectively. Nonlinear equations to determine L_1 and L_2 can then be obtained from Eq. (21) and they are given as

$$kD_1\left(\sinh(\lambda L_1) + \frac{EA\lambda}{\beta}\cosh(\lambda L_1)\right) + \frac{\left(\sinh(\gamma L_1) + \dfrac{EA\gamma}{\beta}\cosh(\gamma L_1)\right) ka \sin(\theta)}{C_5 \sinh(\gamma L) + C_6 \cosh(\gamma L)} - \mu q(L_1) = 0, \tag{27}$$

$$kD_3 \frac{\sinh(\lambda(L_2 - L))}{\cosh(\lambda L)} + \frac{(C_5 \sinh(\gamma L_2) + C_6 \cosh(\gamma L_2)) ka \sin(\theta)}{C_5 \sinh(\gamma L) + C_6 \cosh(\gamma L)} - \mu q(L_2) = 0, \tag{28}$$

where D_1, D_3, C_5 and C_6 are functions of L_1 and L_2, and they are given in Appendix A. Using a similar approach described in Section 2.2 the complete hysteresis curve can be obtained from the solution for θ between 0 and $\pi/2$. The effect of excitation amplitude and frequency are analyzed and compared with the convex normal load case, and the results are presented in Section 3.

3. Results

In the previous sections, one-dimensional microslip models for two different normal load distributions are presented. In the analyses performed in this section, the normal load distribution for the two-region friction

interface is taken as constant, N/L, where N is the total normal load applied, and for the three-region friction interface the following quadratic distribution is used:

$$q(x) = q_0 + q_2 \frac{4x(x-L)}{L^2}, \tag{29}$$

where q_0 and $q_0 - q_2$ indicate the maximum and minimum normal loads acting on the beam, and the total normal load is $N = (q_0 - 2q_2/3)L$.

3.1. Stick–slip transitions

Fig. 6 shows the change of stuck region length, L_1, as a function of temporal variable θ for the two-region friction interface. As predicted from the analysis of the completely stuck system, slip starts from the right end of the beam and propagates towards the left end. Likewise, Fig. 7 shows the changes of L_1 and L_2 as functions of temporal variable θ for the three-region friction interface due to the normal load distribution given in Eq. (29). Slip starts around the middle of the beam and it propagates towards the right and the left ends; furthermore, slip region reaches the right end of the beam first and continues to propagate towards the left end resulting in gross-slip finally.

3.2. Equivalent spring force and damping force

Hysteresis curves, establishing the relationship between the harmonic input displacement and the resulting net force at the right end of the model, are employed to characterize the effectiveness of the frictional constraint. For the two-region friction interface shown in Fig. 4, hysteresis curves for different excitation frequencies are given in Fig. 8, and here ω_c denotes the first natural frequency of the completely stuck system. It is seen that, for low excitation frequencies hysteresis curves are close to each other, which is in agreement with the experimental results obtained by Filippi et al. [12], but there is a small rotation in clockwise direction. For higher frequencies, hysteresis curves rotate more in the clockwise direction and the area enclosed inside them increases.

The equivalent spring force and damping force of a frictional constraint can be obtained from the Fourier coefficients of a hysteresis curve. In this paper, f_s denotes the spring force, being the component in phase with the input displacement, and f_c denotes the damping force, being the 90° out of phase component. Rotation of

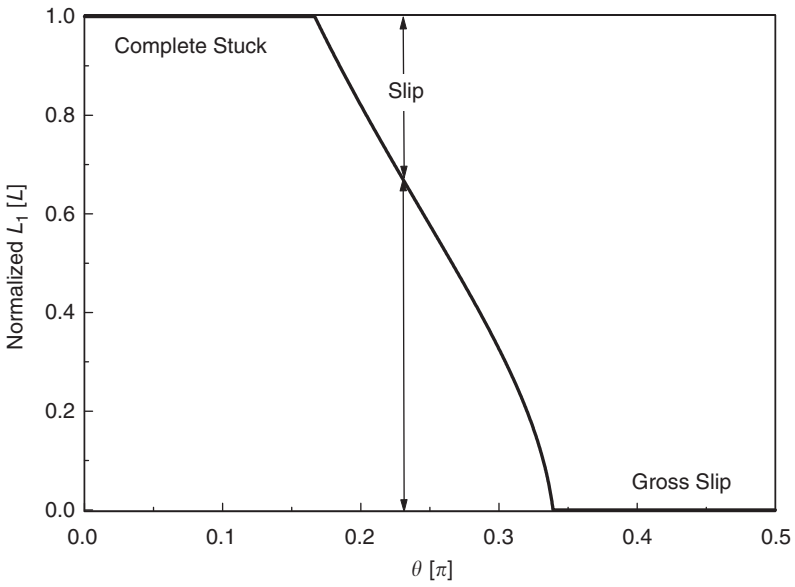

Fig. 6. Temporal change of two-region friction interface.

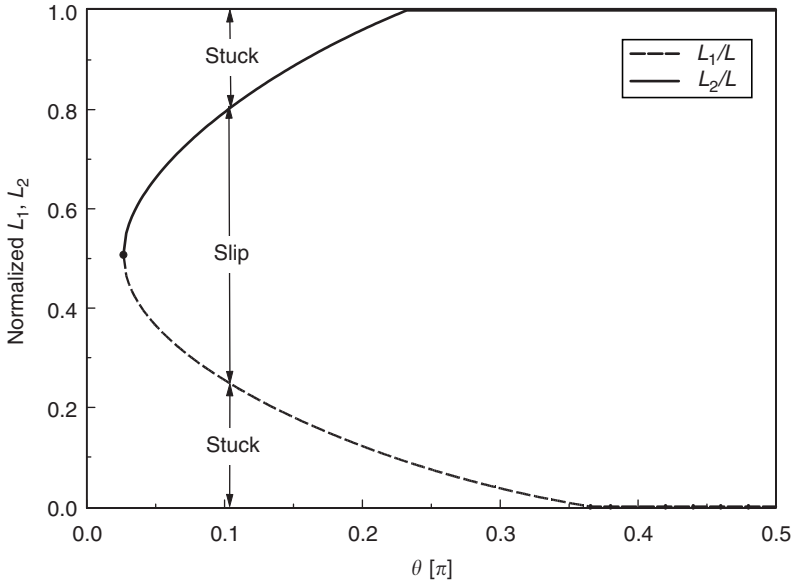

Fig. 7. Temporal change of three-region friction interface: ———, L_1/L; – – – – – –, L_2/L.

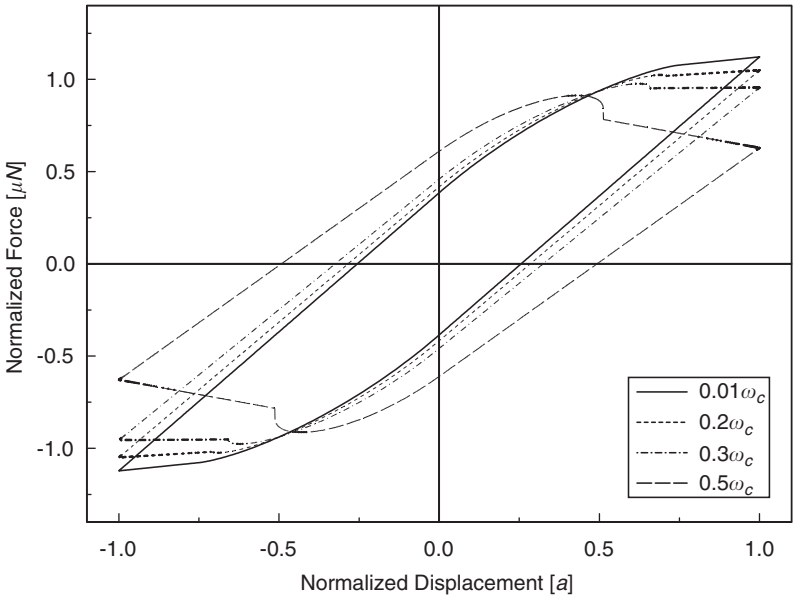

Fig. 8. Effect of excitation frequency on hysteresis: two-region friction interface: ———, $0.01\omega_c$; – – – – –, $0.2\omega_c$; – · – · – · – · – · –, $0.3\omega_c$; – – – – – –, $0.5\omega_c$.

a hysteresis curve in clockwise direction indicates a decrease in Fourier coefficient f_s and increase in area indicates an increase in Fourier coefficient f_c. In Figs. 9 and 10, non-dimensionalized Fourier coefficients $F_s(f_s/k^*a)$ and $F_c(f_c/k^*a)$ vs. normalized displacement amplitude $(a/a_{\min})$ for the two-region friction interface are given for different excitation frequencies, respectively, where k^* is the stiffness of the system when the frequency is zero and $a_{\min}$ is the minimum displacement to cause slip, which is $\mu N/kL$ for this case. It is seen that the non-dimensionalized Fourier coefficient F_s (normalized stiffness) is constant until the slip starts and after this point it decreases with increasing displacement amplitude; moreover, it decreases with increasing excitation frequency. It should be noted that for $\omega = 0.5\omega_c$, the F_s curve can become negative, indicating that the equivalent elastic force is 180° out of phase. On the other hand, the normalized Fourier coefficient F_c

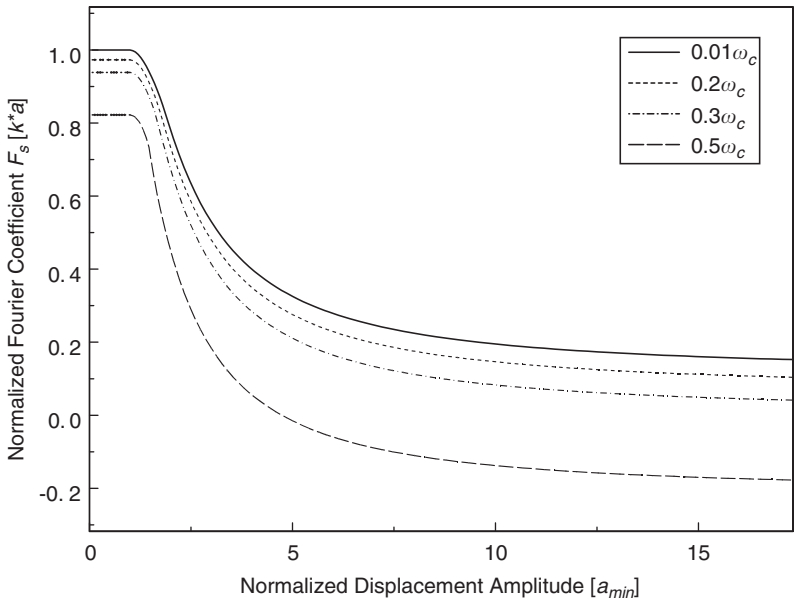

Fig. 9. Effect of excitation frequency on Fourier coefficient F_s: two-region friction interface: ———, $0.01\omega_c$; - - - - - -, $0.2\omega_c$; - · - · - · - · - · - · - ·, $0.3\omega_c$; – – – – – –, $0.5\omega_c$.

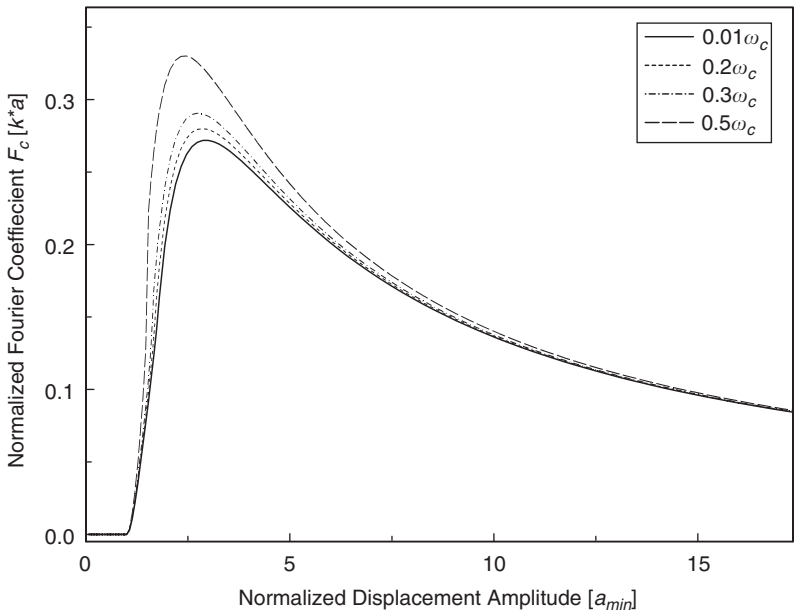

Fig. 10. Effect of excitation frequency on Fourier coefficient F_c: two-region friction interface: ———, $0.01\omega_c$; - - - - - -, $0.2\omega_c$; - · - · - · - · - · - · - ·, $0.3\omega_c$; – – – – – –, $0.5\omega_c$.

(normalized damping) is zero until the slip starts and subsequently, it increases with increasing displacement amplitude, reaches a maximum and becomes stable. In addition to this, although the difference between the curves become insignificant for large displacement amplitudes; for low amplitudes, which is the case for high normal load applications, the Fourier coefficient F_c increases as the excitation frequency increases. In the harmonic response analysis of a structurally damped system, the damping term is included in the stiffness term resulting in a complex stiffness, which can be written as $k(1+\eta i)$; where k, η and i are the stiffness of the

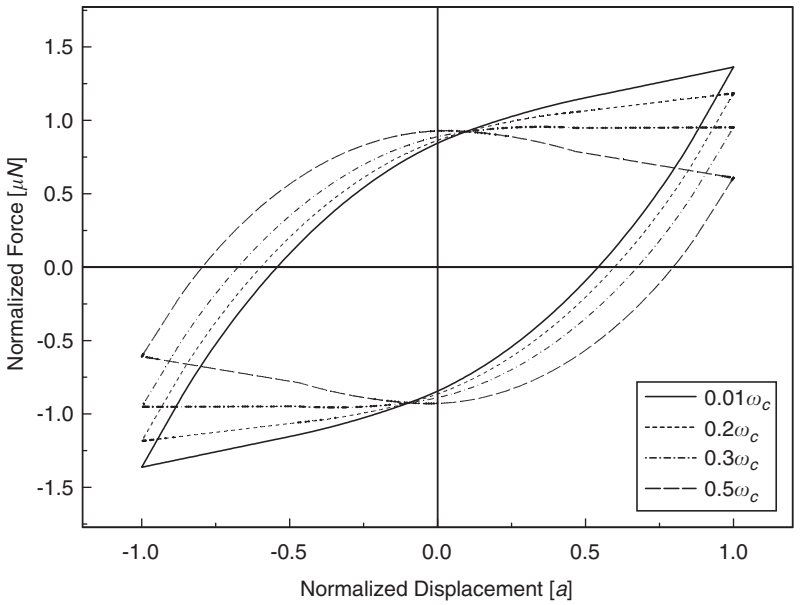

Fig. 11. Effect of excitation frequency on hysteresis: three-region friction interface: ———, $0.01\omega_c$; ------, $0.2\omega_c$; - - - - - - - - - - - -, $0.3\omega_c$; – – – – – –, $0.5\omega_c$.

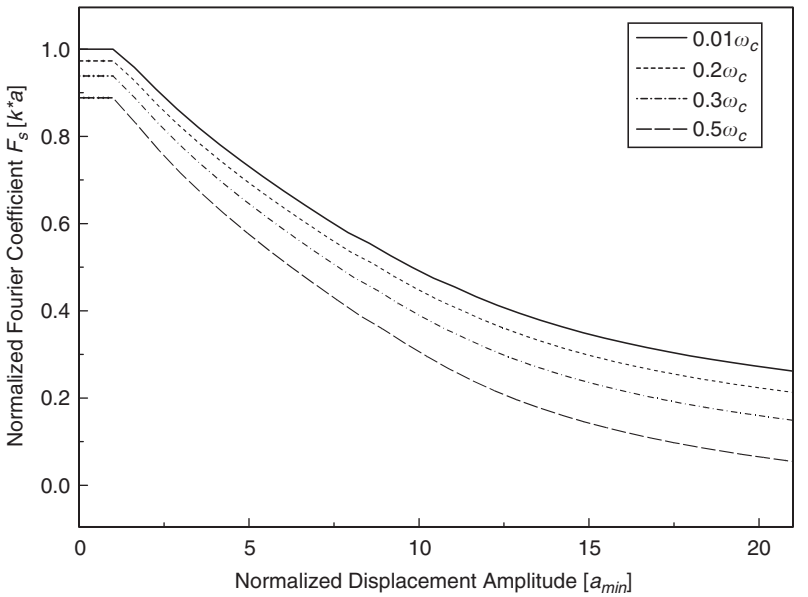

Fig. 12. Effect of excitation frequency on Fourier coefficient F_s: three-region friction interface: ———, $0.01\omega_c$; ------, $0.2\omega_c$; - - - - - - - - - - - -, $0.3\omega_c$; – – – – – –, $0.5\omega_c$.

system, the structural damping coefficient and the imaginary number, respectively. Therefore, the normalized Fourier coefficient F_c can be treated as the structural damping coefficient of the microslip friction model; hence, an increase in F_c expresses an increase in the structural damping of the system.

Hysteresis curves and Fourier coefficients for the three-region friction interface are given in Figs. 11–13, and similar conclusions as in the case of the two-region friction interface can be drawn from them. In the next section, both friction interfaces are compared with each other and differences between them are presented.

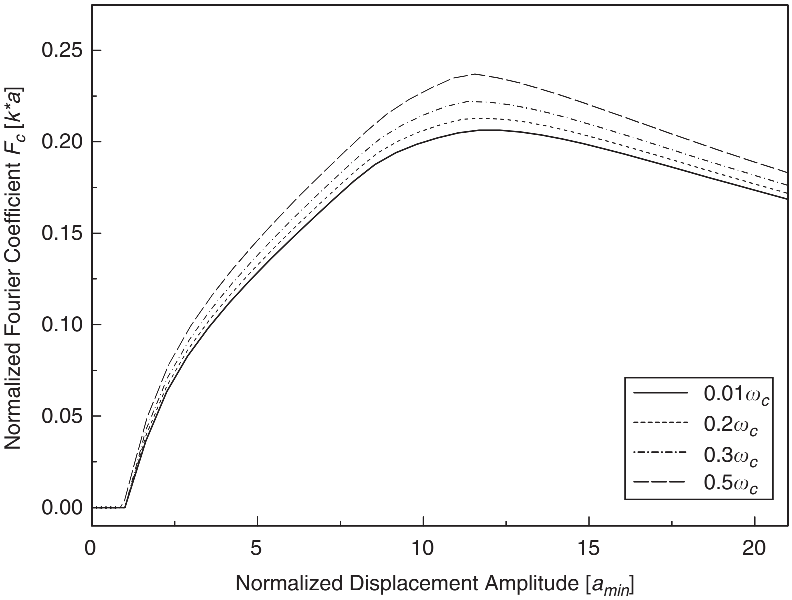

Fig. 13. Effect of excitation frequency on Fourier coefficient F_c: three-region friction interface: ———, $0.01\omega_c$; - - - - - -, $0.2\omega_c$; - · - · - · - · - · - ·, $0.3\omega_c$; — — — — — —, $0.5\omega_c$.

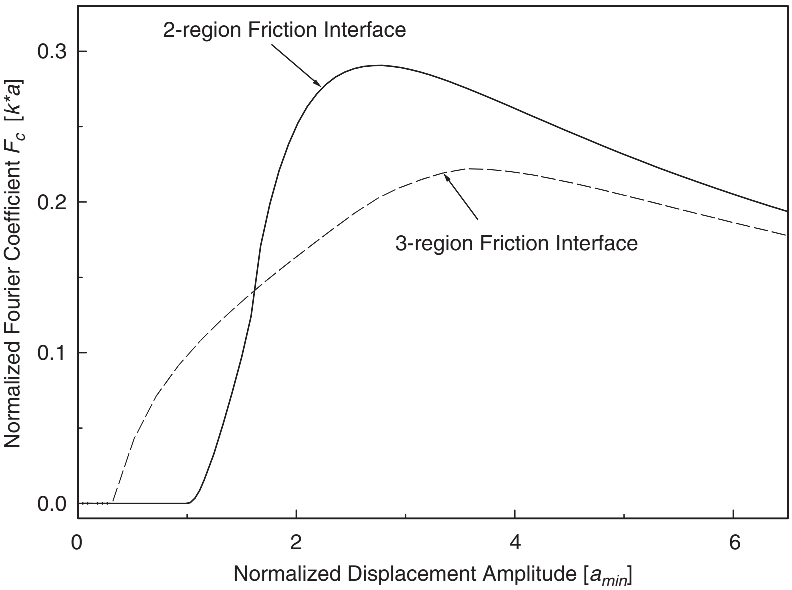

Fig. 14. Comparison of F_c for both friction interfaces ($\omega = 0.3\omega_c$): ———, two-region friction interface; — — — — — —, three-region friction interface.

3.3. Effect of normal load distribution

In order to examine the effect of normal load distribution on microslip of the friction constraint, comparison of the two-region and the three-region friction interfaces are presented in this section. Both friction interfaces are subject to identical total normal load and are analyzed according to the developed approach. The resulting Fourier coefficients F_c and F_s are compared in Figs. 14 and 15, respectively, in which

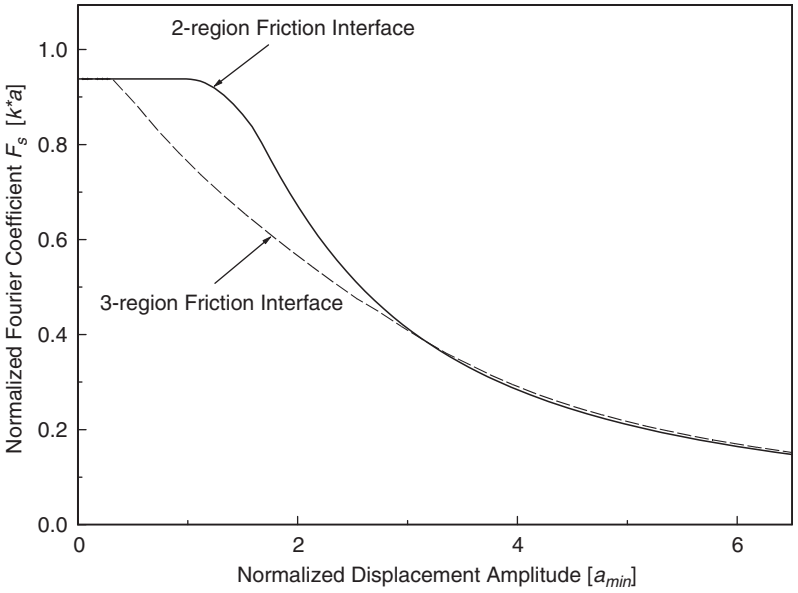

Fig. 15. Comparison of F_s for both friction interfaces ($\omega = 0.3\omega_c$): ———, two-region friction interface; – – – – – –, three-region friction interface.

the displacement amplitude for both interfaces is normalized with respect to $a_{\min}$ of the two-region friction interface. It is seen that due to the nature of concave normal load distribution specified in this comparison, $q_0/(q_0 - q_2) = 12$, the three-region friction interface starts to have partial slip at lower vibration amplitude when compared to the two-region friction interface. In other words, the three-region friction interface starts to generate friction damping, and thus leads to attenuated stiffness, at lower vibration amplitude. However, even though the two-region friction interface requires higher vibration amplitude to start slip, as the vibration amplitude increases the resulting friction damping increases rapidly when compared to that produced by the three-region friction interface. At the same time, after starting slip the equivalent stiffness of the two-region friction interface decreases faster than that of the three-region friction interface, and finally both friction damping and stiffness of the two interfaces become comparable at higher vibration amplitude. This result illustrates that normal load distribution has a significant effect on the microslip characteristics of a friction interface, and accurate prediction of its effect on equivalent stiffness and friction damping is important.

3.4. Comparison with point contact model

A point contact friction model is defined in Fig. 16. The resulting friction damping and equivalent stiffness of this point contact model in terms of vibration amplitude will be compared with those of the two-region friction interface model presented earlier. The unknown stiffness values, β', k' and k_s, are determined in order to satisfy the following three conditions: both models start gross-slip at the same vibration amplitude, and both models have the same equivalent stiffness values in complete stuck and fully slipping states. The resulting Fourier coefficients F_c and F_s are compared in Figs. 17 and 18, respectively, in which the displacement amplitude for both interfaces is normalized with respect to $a_{\min}$ of the two-region friction interface. For high vibration amplitude, it is seen that the results agree with each other well since gross-slip occurs in both models. However, at low vibration amplitude, while the point contact model remains fully stuck, partial slip occurs in the microslip model, and thus increasing friction damping and attenuated stiffness are predicted, which are also observed in experimental results [12]. It is evident that until the gross slip occurs the effects of microslip are very significant.

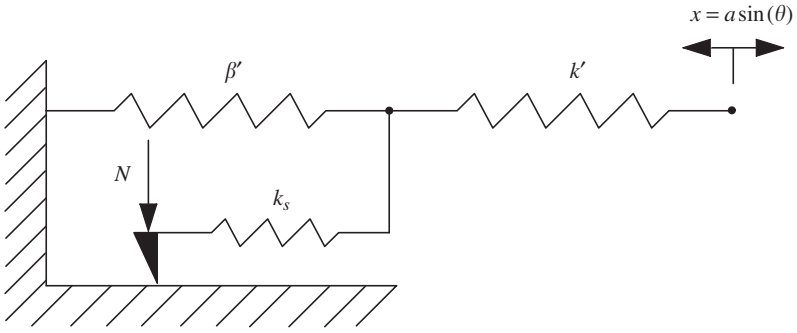

Fig. 16. Equivalent point contact model.

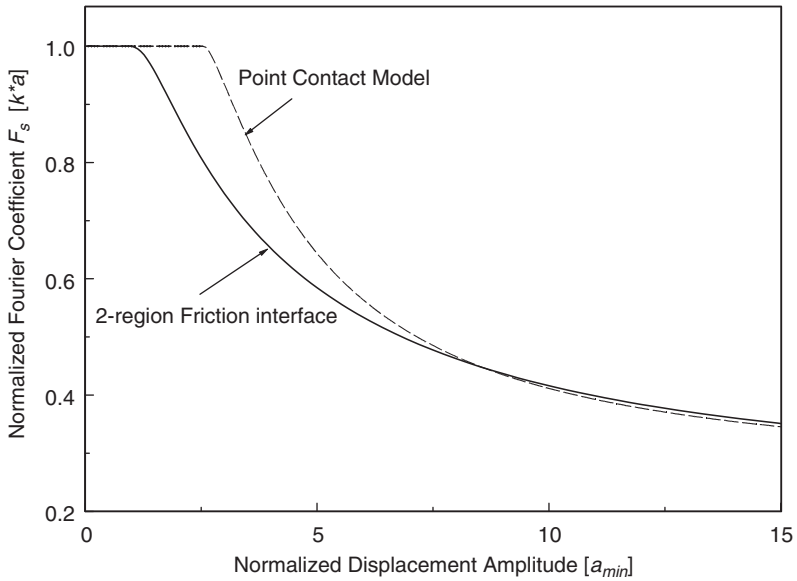

Fig. 17. Comparison of F_s for microslip and point contact models: ———, two-region friction interface; – – – – – –, point contact model.

3.5. Comparison with numerical solution

In order to validate the analytical method developed, time integration is performed on the following nonlinear partial differential equation:

$$EA\frac{\partial^2 u}{\partial x^2} - \tau(u,x) = \rho A\omega^2 \frac{\partial^2 u}{\partial \theta^2},$$

$$\tau(u,x) = \begin{cases} k(u-w) & \text{for stuck,} \\ \operatorname{sgn}\left(\dfrac{\partial w}{\partial \theta}\right)\mu q(x) & \text{for slip,} \end{cases} \tag{30}$$

where $w(x)$ is the displacement of the shear layer as defined in Section 2.2, and the boundary conditions are given in Eq. (2). For the numerical solution technique an implicit finite difference scheme is employed and Fig. 19 shows the change of the normalized stuck region for the two-region friction interface obtained from the analytical and steady-state numerical solutions at low frequency. It is seen that both solutions agree with each other well in the determination of stick–slip transitions.

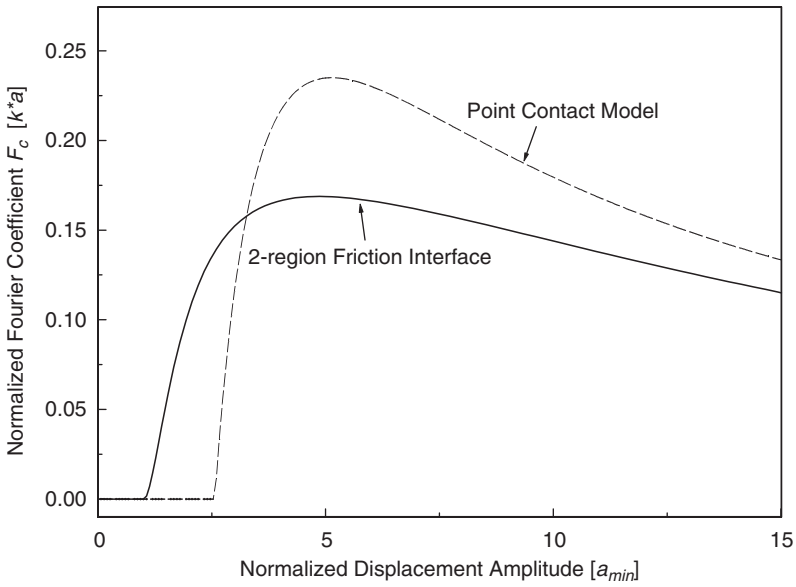

Fig. 18. Comparison of F_c for microslip and point contact models: ———, two-region friction interface; – – – – –, point contact model.

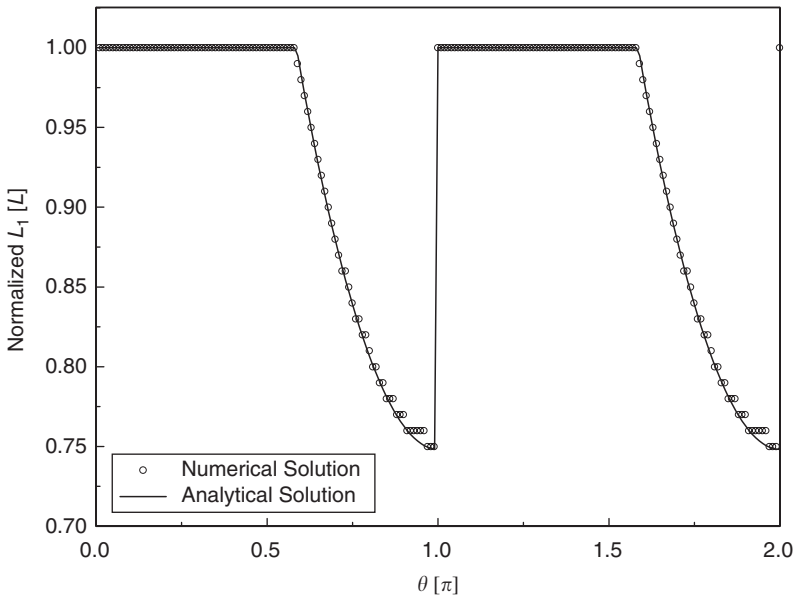

Fig. 19. Comparison of numerical and analytical solutions: ———, analytical solution; o, point contact.

4. Conclusions

A one-dimensional dynamic microslip model is presented in this paper. An analytical approach is developed to determine the stick–slip transitions of the steady-state solution of the frictionally constrained system when subjected to harmonic excitation. In the proposed approach, according to the excitation frequency, a single mode of the system is considered in the steady-state solution for simplicity; consequently, phase difference among spatially distributed points is neglected. The proposed model is analyzed for three different normal load distributions, resulting in two distinct friction interfaces. The two-region friction interface is composed of

a stuck region on the left side and a slip region on the right side of the beam, whereas the three-region friction interface has two stuck regions at the left and the right sides and a slip region in between them. Moreover, the effects of excitation frequency on the resulting hysteresis curves as well as the equivalent stiffness and damping are examined. It is also shown that, even when a friction interface is subjected to identical total normal load, normal load distribution has a significant effect on the equivalent damping and stiffness of the frictionally constrained system.

Although only two-region and three-region friction interfaces are discussed in this paper, other complicated multi-region friction interfaces are possible depending on normal load distribution and excitation frequency. It is possible to extend the developed microslip model to friction interfaces having complicated multiple regions. However, while the number of stick–slip regions increases, the number of unknown variables increases, and so does the number of needed nonlinear equations similar to Eqs. (27) and (28). Moreover, in the proposed approach, according to the excitation frequency, a single mode of the constrained system is employed in the steady-state solution for simplicity; consequently, phase difference among spatially distributed points is neglected. In order to determine the phase difference in terms of spatial distribution, it is necessary to include multiple modes of the system into the solution. This issue will be discussed in future investigation.

Although the microslip friction model presented in this paper is based on a beam model, which is simpler than many engineering structures, it provides a better understanding of the effects of normal load distribution and damper inertia on the stick–slip transitions. For more complicated engineering structures, since numerical methods are often required to obtain the stick–slip transitions and then friction force distributions, the developed method can be used as a basis of comparison, where the numerical results for a simplified model can be verified by the analytical solutions obtained.

Acknowledgement

This material is based on work supported by the GUIde Consortium of the Carnegie-Mellon University, which is sponsored by the Air Force Research Laboratory under Contract no. F33615-01-C-2186. The Consortium Director is Professor Jerry H. Griffin. Any opinions, findings, conclusions, or recommendations expressed herein are those of the authors and do not reflect the views of the Air Force Research Laboratory or Carnegie Mellon.

Appendix A. Unknown coefficients for the three-region friction interface

The coefficients in Eq. (26) are derived and given below.

$$D_1(L_1,L_2)=\frac{-b_2Q_1-(L_2b_2-L_1b_2-b_1)Q_1'+b_2Q_2-b_1Q_2'}{b_2(L_1a_2-a_1)-a_2(L_2b_2-b_1)}, \tag{A.1}$$

$$D_3(L_1,L_2)=\frac{-a_2Q_1+a_1Q_1'+a_2Q_2+(L_1a_2-L_2a_2-a_1)}{b_2(L_1a_2-a_1)-a_2(L_2b_2-b_1)}, \tag{A.2}$$

$$c_0(L_1,L_2)=\frac{(L_2b_2-b_1)(a_2Q_1-a_1Q_1')-(L_1a_2-a_1)(b_2Q_2-b_1Q_2')}{b_2(L_1a_2-a_1)-a_2(L_2b_2-b_1)}, \tag{A.3}$$

$$c_1(L_1,L_2)=\frac{-a_2b_2Q_1+a_1b_2Q_1'+a_2b_2Q_2-a_2b_1Q_2'}{b_2(L_1a_2-a_1)-a_2(L_2b_2-b_1)}, \tag{A.4}$$

$$\begin{aligned}C_5(L_1,L_2)=&-(C_3\sin(\alpha L_2)+C_4\cos(\alpha L_2))\sinh(\gamma L_2)\\&+(C_3\cos(\alpha L_2)-C_4\sin(\alpha L_2))\frac{\alpha}{\gamma}\cosh(\gamma L_2),\end{aligned} \tag{A.5}$$

$$C_6(L_1,L_2) = (-C_3\cos(\alpha L_2) + C_4\sin(\alpha L_2))\frac{\alpha}{\gamma}\sinh(\gamma L_2) + (C_3\sin(\alpha L_2) + C_4\cos(\alpha L_2))\cosh(\gamma L_2), \tag{A.6}$$

where

$$Q(x) = \int_0^x Q'(\xi)\,\mathrm{d}\xi, \quad Q'(x) = \int_0^x \frac{\mu}{EA}\,q(\xi)\,\mathrm{d}\xi, \tag{A.7}$$

$$Q_1 = Q(L_1), \quad Q_1' = Q'(L_1), \tag{A.8}$$

$$a_1 = a_1(L_1) = \sinh(\lambda L_1) + \frac{EA\lambda}{\beta}\cosh(\lambda L_1), \tag{A.9}$$

$$a_2 = a_2(L_1) = \lambda\left(\cosh(\lambda L_1) + \frac{EA\lambda}{\beta}\sinh(\lambda L_1)\right), \tag{A.10}$$

$$Q_2 = Q(L_2), \quad Q_2' = Q'(L_2), \tag{A.11}$$

$$b_1 = b_1(L_2) = \frac{\sinh(\lambda(L_2-L))}{\cosh(\lambda L)}, \tag{A.12}$$

$$b_2 = b_2(L_2) = \frac{\lambda\cosh(\lambda(L_2-L))}{\cosh(\lambda L)}, \tag{A.13}$$

$$C_3 = C_3(L_1) = \left(\sin(\alpha L_1) + \frac{EA\lambda\gamma}{\alpha\beta}\cos(\alpha L_1)\right)\sinh(\gamma L_1) + \left(\frac{EA\lambda}{\beta}\sin(\alpha L_1) + \frac{\gamma}{\alpha}\cos(\alpha L_1)\right)\cosh(\gamma L_1), \tag{A.14}$$

$$C_4 = C_4(L_1) = \left(\cos(\alpha L_1) - \frac{EA\lambda\gamma}{\alpha\beta}\sin(\alpha L_1)\right)\sinh(\gamma L_1) + \left(\frac{EA\lambda}{\beta}\cos(\alpha L_1) - \frac{\gamma}{\alpha}\sin(\alpha L_1)\right)\cosh(\gamma L_1). \tag{A.15}$$

References

[1] C.-H. Menq, J.H. Griffin, A comparison of transient and steady state finite element analyses of the forced response of a frictionally damped beam, *Journal of Vibration, Acoustics, Stress and Reliability in Design* 107 (1985) 19–25.

[2] S. Chen, A. Sinha, Probabilistic method to compute the optimal slip load for a mistuned bladed disk assembly with friction dampers, *Journal of Vibration and Acoustics* 112 (1990) 214–221.

[3] J.H. Wang, W.K. Chen, Investigation of the vibration of a blade with friction damper by HBM, *Journal of Engineering for Gas Turbines and Power* 115 (1993) 294–299.

[4] K.Y. Sanliturk, D.J. Ewins, R. Elliott, J.S. Green, Friction damper optimization: simulation of rainbow tests, *Journal of Engineering for Gas Turbines and Power* 123 (2001) 930–939.

[5] E. Cigeroglu, Nonlinear Vibration Analysis of Bladed Disks with Dry Friction Dampers, MS Thesis, Middle East Technical University, Ankara, 2002.

[6] C.-H. Menq, J. Bielak, J.H. Griffin, The influence of microslip on vibratory response—part I: a new microslip model, *Journal of Sound and Vibration* 107 (1986) 279–293.

[7] W. Lu, Modeling of Microslip Friction and Design of Frictionally Constrained Turbine Blade Systems, PhD Thesis, The Ohio State University, 2001.

[8] C.-H. Menq, J. Bielak, J.H. Griffin, The influence of microslip on vibratory response—part II: a comparison with experimental results, *Journal of Sound and Vibration* 107 (1986) 295–307.

[9] G. Csaba, Forced response analysis in time and frequency domains of a tuned bladed disk with friction dampers, *Journal of Sound and Vibration* 214 (1998) 395–412.
[10] K.Y. Sanliturk, M. Imregun, D.J. Ewins, Harmonic balance vibration analysis of turbine blades with friction dampers, *Journal of Vibration and Acoustics* 119 (1997) 96–103.
[11] F.P. Bowden, D. Tabor, *The Friction and Lubrication of Solids*, Clarendon Press, Oxford, 1950.
[12] S. Filippi, A. Akay, M.M. Gola, Measurement of tangential contact hysteresis during microslip, *Journal of Tribology* 126 (2004) 482–489.
[13] Y. Song, C.J. Hartwigsen, D.M. McFarland, A.F. Vakakis, L.A. Bergman, Simulation of dynamics of beam structures with bolted joints using Iwan beam elements, *Journal of Sound and Vibration* 273 (2004) 249–276.